JOURNAL OF GEOPHYSICAL RESEARCH, VOL. 101, NO. A12, PAGES 26,741–26,758, DECEMBER 1, 1996

F region climatology during the SUNDIAL/ATLAS 1 campaign of March 1992: Model-measurement comparisons and cause-effect relationships

E. P. Szuszczewicz,[1] D. Torr,[2] P. Wilkinson,[3] P. Richards,[2] R. Roble,[4] B. Emery,[4] G. Lu,[4] M. Abdu,[5] D. Evans,[6] R. Hanbaba,[7] K. Igarashi,[8] P. Jiao,[9] M. Lester,[10] S. Pulinets,[11] B.M. Reddy,[12] P. Blanchard,[1] K. Miller,[13] J. Joselyn[6]

Abstract. We present the first joint comparison of global measurements of *F* region characteristics with three models used widely in the specification of the ionospheric-thermospheric system. The models, the International Reference Ionosphere (IRI), the field line interhemispheric plasma (FLIP) model, and the Thermospheric-Ionospheric General Circulation Model (TIGCM), represent a unique set of capabilities with major differences in approaches to the prevailing physics and different levels of computational complexity. The database was developed by a global network of 53 ionosonde stations operating around-the-clock for the period March 22 through April 4, 1992 in collaboration with the ATLAS 1 mission. The emphasis is on the *F* region characteristics of peak heights (h_mF_2) and densities (N_mF_2), their climatological (i.e., average) behavior during the ATLAS 1 period, and associated cause-effect relationships. We explore latitudinal and local time variations with attention to the influences of meridional winds and plasmaspheric fluxes in the maintenance of different domains in the ionospheric-thermospheric system. We find that all three models tend to underestimate the values of h_mF_2 and N_mF_2 with the largest discrepancies in N_mF_2 resulting in the FLIP and TIGCM representations at night. These discrepancies can grow to levels as large as 110% near 0400 LT, a "rediscovery" of the old but unsettled issue of maintenance of the nighttime ionosphere. This nighttime discrepancy is traceable in first order to model underestimates of prevailing meridional winds. The contributions of plasmaspheric fluxes are also considered, with the conclusion that they are of secondary importance, but substantially more work is necessary to uniquely quantify their role. In contrast to their nighttime characteristics, the FLIP and TIGCM generally have excellent agreement (i.e., 6±6%) with daytime observations of N_mF_2, and the IRI tends to underestimate the observed values of N_mF_2 by a nominally LT-insensitive level of 28±6%. Other campaign results are reviewed in this issue, with a focus on regional responses to the prevailing conditions and their characterization in terms of latitudinal distributions of *F* region heights and densities.

1. Introduction

1.1. Perspectives on the Investigation

There are a number of trends evolving in experimental and theoretical aspects of solar-terrestrial physics. These may be considered to include the following: (1) the organization of characteristic responses within the framework of space weather and climatology; (2) an increased emphasis on remote sensing techniques; and (3) dependence on large-scale numerical models for predictions or deductions about cause-effect relationships that are not readily measured.

Within the concept of "space weather and climatology" [*Sime and Behnke*, 1994; *Siscoe et al.*, 1994; *Szuszczewicz*, 1995], climatology deals with "average" conditions that result under a set of large-scale slowly changing (i.e., weeks, to months, to years) forcing functions. On the other hand, weather addresses drivers and system responses framed within their hour-to-hour and day-to-day variability. Embodied in these concepts is the idea of "predictions" that encompass the scientifically rigorous position that accurate predictions of weather and climatology are the ultimate test of understanding. As space science matures, the logic of such a focus looms as increasingly important.

The trend toward an ever-increasing reliance on large-scale numerical models stems in part from the premise that no measurement program will ever be able to define completely the input and output parameters in a given cause-effect chain of geophysical events. Thus theory, and in particular comprehensive first-principle models, must be relied upon to make deductions where data are not available and to provide

[1]Science Applications International Corporation, McLean, Virginia.
[2]University of Alabama, Huntsville.
[3]IPS Radio and Space Services, West Chatswood, Australia.
[4]National Center for Atmospheric Research, Boulder, Colorado.
[5]Instituto Nacional de Pesquisas Espaciais, Sao Paulo, Brazil.
[6]National Oceanic and Atmospheric Administration, Boulder, Colorado.
[7]France Telecom/Centre National D'etudes de Telecommunications, Lannion, France.
[8]Communications Research Lab, Tokyo, Japan.
[9]China Research Institute of Radio Propagation. Henan, China
[10]Department of Physics, University of Leicester, Leicester, England.
[11]IZMIRAN, Moscow, Russia.
[12]National Physical Laboratory, New Delhi, India.
[13]Center for Atmospheric and Space Sciences, Utah State University, Logan, Utah

Paper number 96JA01774
0148-0227/96/96JA-01774$09.00

insight into the physical processes of importance. However, theoretical models are accurate only to the extent that the fundamental processes are adequately understood, mathematically represented, and empirically bounded. Therefore there is the need to use experimental data, in particular global-scale data, to validate individual models, quantify their accuracies, impose self-consistency, and identify regions for improvement.

The trend toward an increased emphasis on remote sensing techniques is motivated in part by the number of geophysical or solar-terrestrial domains that are difficult or impossible to routinely access with "in situ" techniques. This trend also appears to be motivated by a perspective that remote sensing techniques can provide more global views of phenomenological domains and therefore perform (arguably) more effectively than satellite- or rocket-borne "in situ" diagnostics. Such has been the thrust of the ATLAS 1 mission [*Torr et al.*, 1993; *Fennelly et al.*, 1994], the current series of shuttle-borne GLO investigations [*Broadfoot et al.*, 1992; *Gardner et al.*, 1995], and the planned NASA/TIMED satellite program. Many of the remote sensing techniques however are integrated line-of-sight measurements that require inversion procedures that are forced to make assumptions about the physical processes and local particle distributions giving rise to their respective observables. Therefore there is often need for coincident ground-truth measurements that provide benchmarks for the remote sensing procedures as well as spatial and temporal continuity between and among the along-track remote-sensing database.

This investigation embodies all three trends. It addresses the issue of cause-effect terms as manifested in the global-scale climatology of the ionospheric-thermospheric system during the solar-maximum equinoctial period of the ATLAS 1 period. It also addresses the issue of model testing and verification, with an emphasis on quantifying agreement and disagreement with observations as well as between and among various models. The approach also focuses on remote sensing techniques and necessary elements of ground-truth with a global network of 53 SUNDIAL ionosondes operating around-the-clock for the entire period of the ATLAS 1 mission (March 23 through April 2, 1992).

1.2. Investigative Components

ATLAS 1 was launched on March 23, 1992, at 1301 UT into a 57° inclination 297-km circular orbit with a complement of photometric devices covering atomic, molecular and ionic emissions over the wavelength regime from the EUV through the IR [*Torr et al.*, 1993]. The intent was to measure the density and temperature distributions of the neutral and ion constituents from mesospheric altitudes up through the F-region. This was to be the first of a series of flights which would develop one of the first data sets dealing with the mesosphere and make available ionospheric and thermospheric results for the test and verification of developing large-scale models.

The ground-based SUNDIAL component had a separate but synergistic set of continuing objectives that supported the ATLAS 1 interests while developing a synoptic view of the global-scale ionospheric-thermospheric (I-T) system. Among those objectives has been the development of a worldwide database [*Szuszczewicz et al.*, 1988, 1990, 1993] for an empirical specification of the state and condition of the I-T system and its weather and climatology as influenced by seasonal, solar cycle, diurnal and storm time controls. Working with that database, the objectives also contributed to the development of a predictive capability through the test, verification and validation of empirical and first principle models. Past SUNDIAL efforts have included the empirically derived International Reference Ionosphere (IRI) [*Rawer*, 1981; *Rawer and Ramanamurty*, 1985; *Schunk and Szuszczewicz*, 1988] and the auroral oval models of Feldstein and the Television and Infrared Observation Satellite (TIROS) and Defense Meteorological Satellite Programs (DMSP) [*Szuszczewicz et al.*, 1993]. Test and validation efforts have also included a number of first-principle models: the time-dependent ionospheric model of Utah State [*Wilkinson et al.*, 1988; *Sica et al.*, 1990], the Thermospheric-Ionospheric General Circulation Model TIGCM of the National Center for Atmospheric Research (NCAR) [*Wilkinson et al.*, 1992; *Szuszczewicz et al.*, 1995a] and the Rice Convection Model [*Spiro et al.*, 1988; *Fejer et al.*, 1990].

In this investigation we concentrate on the IRI, the NCAR/TIGCM, and the Field Line Interhemispheric Plasma (FLIP) [*Richards et al.*, 1994a]) models. They represent a unique set of capabilities that reflect major differences in approaches to the representation of the prevailing physics along with a substantial difference in computer requirements. The IRI, FLIP, and TIGCM are PC, work station, and Cray based, respectively. The IRI is purely empirical in its approach. The FLIP code is a one-dimensional model which inputs thermospheric controls by incorporating composition from the Mass Spectrometer and Incoherent Radar (MSIS) model [*Hedin*, 1987] and meridional winds from empirical models or from radars, ionosondes or Fabry-Perot interferometers. The NCAR/TIGCM might (arguably) be considered the closest to an all first-principles model since it self-consistently solves the system of equations which defines the coupled I-T domain. Rigorously speaking however, it is not entirely first principle since it invokes the empirically defined electric field model of *Richmond et al.* [1980] and the assimilative mapping of ionospheric electrodynamics (AMIE) specification [*Richmond*, 1992; *Lu et al.*, 1995] of particles, fields, and currents at high latitudes. We present here the very first joint comparison of all three approaches against the global database with a perspective that highlights the differences in the approaches and the relative agreement with the data. We focus on climatology, drawing perspectives on diurnal variability, thermospheric wind controls, plasmaspheric fluxes, and phenomenological domains. We also include a perspective on the overall characteristics of the *F* region ionosphere as manifested during the March 23 to April 2, 1992, SUNDIAL/ATLAS 1 period.

2. The Database and the Models

2.1 The Data

2.1.1 Prevailing conditions. The SUNDIAL/ATLAS 1 campaign was conducted during the first equinoctial period of the descending phase of solar cycle 22. The months of March and April showed a dramatic decrease in energetic solar events compared with previous months. While there were 49 energetic solar X ray events (M class or higher) in February, there were only four in March and eight in April. Four M class

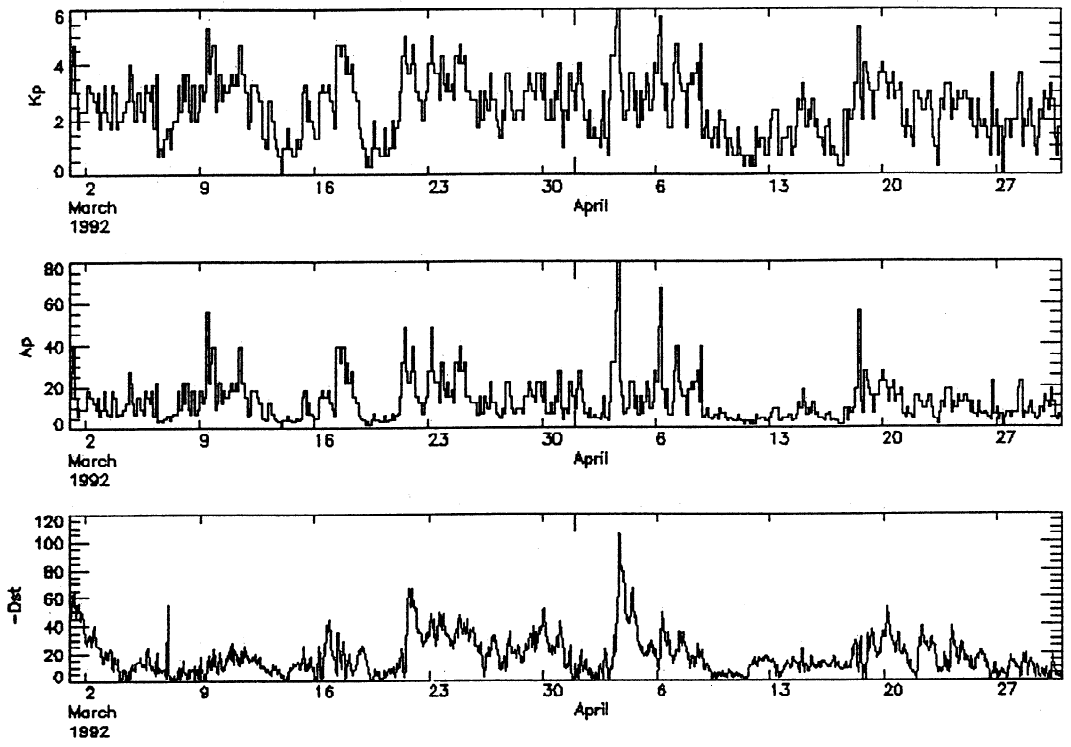

Figure 1. Activity indices (top) *Kp*, (middle) *Ap* and (bottom) *Dst* for March and April 1992. Note that *-Dst* is plotted.

events occurred during the ATLAS 1 period: one on March 31 at 1545 UT and three on April 1 at 0100, 1017, and 1748 UT. The average uncorrected 10.7 cm flux for the ATLAS 1 period was 182, compared with averages of 171 and 158 for the entire months of March and April, respectively.

Solar wind observations for the campaign period were not available through March 26. But observations for the remainder of the campaign showed rather steady behavior with the solar wind velocity in the 325-425 km/s domain, and densities holding relatively steady near 10/cm^3. There was a brief period in which the density was enhanced by a factor of 3 (around 2100-2400 UT on March 31) but that was not accompanied by any increased velocity.

To develop a perspective on geomagnetic activity for the season and phase of the solar cycle in which the investigation took place, we present in Figure 1 the Kp, Ap and $-Dst$ indices. The three panels in that figure, top-to-bottom, show *Kp*, *Ap*, and *-Dst*, respectively, for March and April 1992. The Kp and Ap values, 3±2 and 20±15, respectively, for the ATLAS 1 period (March 23 to April 2) were generally typical for the entire month of March. Overall, the conditions can be described as moderately active.

In the bottom panel of Figure 1 it can be seen that $-Dst$ values were generally depressed during the ATLAS 1 period with values less than -50 considered "stormy" [*Taylor et al.*, 1994; *Kamide*, 1994]. These results show that the entire ATLAS 1 period occurred during the recovery phase of a storm that took place at about 2300 UT on March 21. That recovery can be seen to be populated by a number of substorms [*Lester et al.*, 1995] with *Dst* values gradually returning to zero on April 2, the quietest day of the entire campaign.

One final perspective on energy inputs and activity levels was provided by the interhemispheric power and activity indices determined by measurements on the NOAA/TIROS satellite [*Foster et al.*, 1986]. Those results corroborate the generally active nature of the ATLAS 1 period. The NOAA/TIROS activity indices were routinely between 4 and 8, with only two brief excursions to the maximum level of activity (i.e., 10) at about 1700 UT on March 24 and 0400 UT on March 29.

In companion papers, substorm influences on high-latitude conductivities are investigated during the periods March 27 and 30-31 [*Lester et al.*, this issue], while the overlapping Geophysical Environmental Modeling (GEM) campaign days of March 28 and 29 are studied from perspectives focused on high-latitude inputs and substorms [*Lu et al.*, this issue] and global-scale ionospheric-thermospheric variability [*Emery et al.*, this issue]. These studies, along with the investigations of *Wilkinson et al.* [this issue], *Abdu et al.* [this issue], and *Pulinets et al.* [this issue], who focus on ionospheric weather and climatology in the 115°-165° longitude zone, at equatorial latitudes, and in the Russian sector, respectively, represent the ground-based measurement and modeling component of the campaign.

2.1.2. The ionosonde database. The ground-based data were acquired by the global network of 53 ionosonde stations listed in Table 1, complemented by radar observations at EISCAT, Sondrestrom, Millstone Hill, Arecibo, and Jicamarca. While the radar observations operated only on a short schedule, the ionosonde measurements were carried out around-the-clock for the entire ATLAS 1 period with emphasis here on measured F region characteristics (f_0F_2 and $M(3000)F_2$). The parameter $M(3000)F_2$ is the transmission factor from which the real height h_mF_2 of the F_2 peak can be derived [*Dudeney*, 1983] and f_0F_2 is the critical frequency of the F_2 peak. Throughout the text f_0F_2 will be used

TABLE 1. SUNDIAL/ATLAS 1 Stations

Name	Latitude	Longitude
Ahmedabad	23.0	72.6
Akita	39.7	140.1
Arkhangelsk	64.6	40.5
Buenos Aires	-34.6	301.7
Cachoeria Paulista	-22.7	315.0
Canberra	-35.3	149.0
Canton	23.1	113.3
Chanchun	43.8	125.3
Chung-Li	25.0	121.2
Chungking	29.6	106.5
Churchill	58.7	265.8
Dakar	14.8	242.6
Darwin	-12.3	130.9
Fortaleza	-3.7	321.0
Hankou	30.7	114.3
Hobart	-42.9	147.3
Irkutsk	52.5	104.0
Kaliningrad	54.7	20.6
Karaganda	49.8	73.1
Khabarovsk	48.5	135.2
Kiruna	67.8	20.4
Kodaikanal	10.2	77.5
La Reunion	-21.2	55.6
Lanchou	36.1	103.8
Lannion	48.8	356.6
Leningrad	60.0	30.7
Lycksele	64.6	18.8
Magadan	60.1	151.0
Manchouli	49.6	117.4
Moscow	55.5	37.3
Mundaring	-32.0	116.2
Norfolk Is.	-29.0	168.0
Novosibirsk	54.6	83.2
Okinawa	26.3	127.8
Ottawa	45.4	284.1
Ouagadougou	12.4	358.5
Peiping	40.0	116.3
Poitiers	46.6	0.3
Resolute Bay	74.7	265.1
Rome	41.8	12.5
Sverdlovsk	56.7	61.1
Tahiti	-17.7	210.7
Tashkent	41.3	69.0
Townsville	-19.6	146.8
Trivandrum	8.2	77.0
Tunguska	61.6	90.0
Uppsala	59.8	17.6
Ushuaia	-54.8	291.7
Vanimo	-2.7	141.3
Wakkanai	45.4	141.7
Waltair	18.0	83.0
Wulumuqui	43.7	87.6
Yamagawa	31.2	130.6

synonymously with the peak density of the F_2 region (i.e., N_mF_2) since f_0F_2[Hz] = $8.9(10^3)[N_mF_2(\text{cm}^{-3})]^{1/2}$. Accuracy in the values of f_0F_2 and $M(3000)F_2$ is discussed in *Wilkinson* [1978] and potential errors in the transformation of $M(3000)F_2$ to h_mF_2 are discussed in *Wilkinson et al.* [this issue]. These references report that accuracy in f_0F_2 is typically 0.1 MHz (or equivalently 125 cm^{-3} in the density of the F_2 peak, N_mF_2) and inaccuracies in $M(3000)F_2$ can amount to random errors in h_mF_2 not in excess of ±10 km.

Figures 2 and 3 provide an introductory perspective on observed ground-based responses of the ionosphere to the prevailing solar-terrestrial conditions. Figure 2 presents a subset of "events" primarily observed in the northern hemisphere. These include a series of substorms, as identified in the European sector by the successor to the European incoherent scatter (EISCAT) magnetometer cross [*Luhr et al.*, 1984], the midlatitude Subauroral Magnetometer Network (SAMNET) [*Yeoman et al.*, 1990], and by positive and negative storm phases in the Russian and French ionosonde results.

In general, "stormy" ionospheric conditions were observed at high latitudes, while nominally quiet characteristics were observed at mid- and equatorial latitudes. This can be seen to some extent in Figure 3 which displays diurnal plots of f_0F_2 (and N_mF_2) for pairs of stations in the Russian/East-African, the Asian/Australian, and the American sectors. (The f_0F_2 values are expressed in megahertz throughout the paper with f_0F_2 = 5, 10 and 15 MHz equal to N_mF_2 = 0.3, 1.3 and $2.8(10)^6$ cm^{-3}, respectively. For convenience, the N_mF_2 scaling is displayed along the right-hand ordinates in Figure 3.) These station pairs (each pair formed by a high-northern and low-southern latitude site in approximately the same longitude sector) are Moscow/La Reunion, Magadan/Townsville, and Ottawa/Buenos Aires, respectively. The plots present the following: 1) the hourly observations as solid dots, 2) the average diurnal characteristic determined for the entire campaign period as a solid line, and 3) the IRI specification as a dashed line. It can be seen in the figure that the high-latitude sites show irregular day-to-day behavior. Note, for example, the negative and positive storm phases at Moscow on March 25 and 27, respectively. By contrast, the mid-latitude stations show very regular behavior, with the day-to-day characteristics virtually identical with the campaign-period average.

All ionosonde data were subjected to three levels of editing and quality control: the first by regional coordinators (e.g. S. Pulinets for Russian data, M.A. Abdu for South American data, etc.), the second at the initial staging center for data fusion (the Ionospheric Prediction Service, at Sydney, Australia), and the third at the SAIC Data Archive and Analysis Center where errors and inconsistencies were screened on regional and global bases using special purpose data handling and visualization tools [*Szuszczewicz et al.*, 1995b]. This process mitigated possible contamination of subsequent model-measurement comparisons by spurious or otherwise erroneous data.

2.2. The Models

2.2.1 The IRI. Currently the empirically derived IRI model is the most used and widely-tested climatological specification of the global ionosphere [*Rawer*, 1981; *Rawer and Ramanamurty*, 1985; *Schunk and Szuszczewicz*, 1988]. It describes the E and F regions of the ionosphere in terms of location (geographic or geomagnetic), time, solar activity (sunspot number), and season (month). By definition it is based on accumulated data, including critical frequencies (f_0E, f_0E_S, f_0F_1, and f_0F_2), altitudes of peak concentrations (h_mE, h_mF_1, and h_mF_2), half thicknesses of the individual layers, and

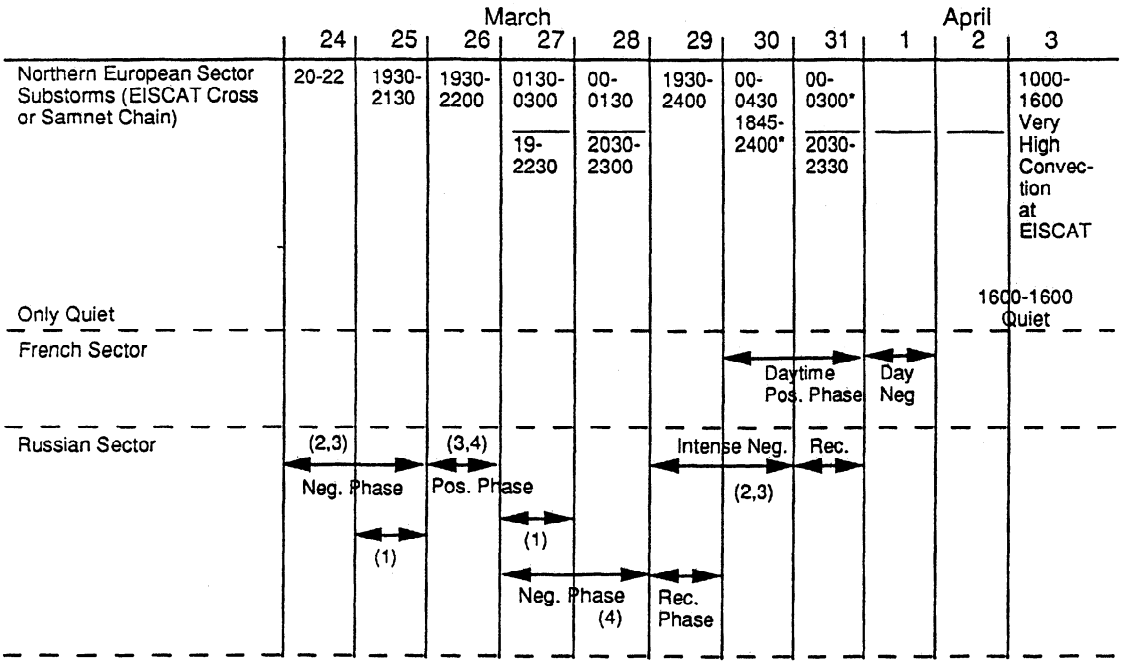

Figure 2. SUNDIAL-ATLAS "events" with specific station observations noted as 1, Moscow; 2, St. Petersburg; 3, Arkhangelsk; 4, Sverdiovsk; and 5, Novosibirsk.

ion composition and plasma temperatures. The database forming the foundation of the IRI was compiled from ionosondes, topside sounders, incoherent scatter radars, and in situ satellite and rocket profiles (wherever available). Averaged profiles were synthesized and analytical fits developed, with the end product representing an intelligent mix of empiricism, physics, extrapolation, and intuition. In general, the quality of the IRI representation of actual climatological conditions is directly related to available data, its global distribution, parameter space coverage, time base, and accuracy. Obvious gaps in the database include ocean regions and ionogram definition of the *E-F* region valley.

Notwithstanding the limitations of the IRI, it can (and does) provide a valuable resource that includes a broad experience base in ionospheric profiling and data archiving. Its output provides a global specification not only on the macroscale features of electron density but also on the ion and electron temperatures and the ion composition. These additional features make the IRI an attractive model for comparison with satellite and ground-based data as well as first-principle codes.

The IRI is an evolutionary model, with its primary emphasis being an attempt at a global-scale representation of observations. In this regard the IRI makes its limitations clear, particularly with regard to the relative paucity of ion composition results. Work has continued in improving its specification of the topside domain [*Bilitza*, 1994], its specification of plasma temperatures and ion composition [*Bilitza et al.*, 1992a], and its specification of global and mesoscale electron density distributions [*Bilitza et al.*, 1992b; *Szuszczewicz et al.*, 1990, 1993]; while its inaccuracies at high latitudes can be partially mitigated by inclusion of the NOAA/TIROS, DMSP, or Feldstein auroral oval models [*Szuszczewicz, et al.*, 1993, and references therein].

For comparisons in this investigation the IRI was run with the observed smoothed sunspot number of 108 and a seasonal behavior equivalent to the end of March and beginning of April (i.e., month = 3.5), a period conforming closely to the SUNDIAL/ATLAS-1 campaign.

2.2.2. The FLIP model. The field line interhemispheric plasma model has been described previously by *Richards and Torr* [1988] and more recently by *Torr et al.* [1990] and *Richards et al* .[1994a]. The main component of this one-dimensional model calculates the plasma densities and temperatures along entire magnetic flux tubes from 80 km in the northern hemisphere through the plasmasphere to 80 km in the southern hemisphere using a tilted dipole approximation to the Earth's magnetic field. The FLIP model solves the continuity and momentum equations for O^+, H^+, N^+, and He^+.

The electron and ion temperatures are obtained by solving the energy equations [*Schunk and Nagy*, 1978] with electron heating due to photoelectrons provided by a solution of the two-stream photoelectron flux equations using the method of *Nagy and Banks* [1970]. The solutions have been extended to encompass the entire field line on the same spatial grid as the ion continuity and momentum equations.

Once all the interhemispheric solutions have been determined, densities of NO^+, O_2^+, N_2^+ (v=0-6), $O^+(^2D)$, and O (^2P) are obtained from local chemical equilibrium. Then diffusion equations are solved on separate vertical grids in both hemispheres to obtain the densities of the minor neutral species $N(^2D)$, $N(^4S)$, NO, and vibrationally excited N_2 on vertical grids extending from 80 km to about 500 km in each hemisphere.

The FLIP model includes provisions to solve the continuity and momentum equations for the first six vibrational levels of N_2 in order to take into account the strong dependence of the $O^+ + N_2 \rightarrow NO^+ + N$ reaction rate

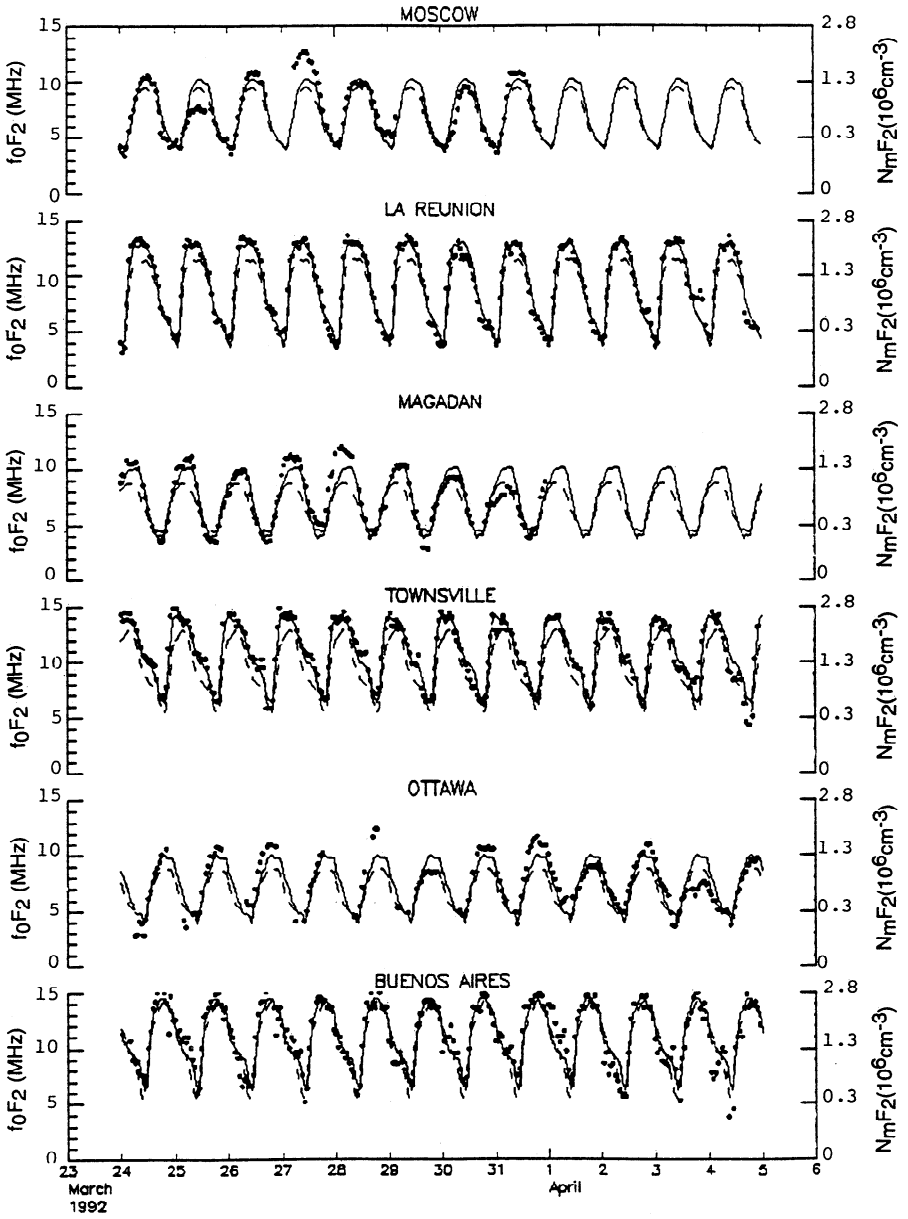

Figure 3. Diurnal characteristics of measured values of f_0F_2 (in megahertz) at six of the ionosonde stations covering the period March 24 through April 4, 1992. Dots, solid curve, and dashed curve represent the data, the average diurnal behavior for the period, and the IRI "predictions", respectively. Note that f_0F_2 (hertz) = $8.9(10^3)$ $(N_mF_2(\text{cm}^{-3}))^{1/2}$ with the right-hand abscissa showing the conversion of f_0F_2 = 5, 10, and 15 MHz to N_mF_2 = 0.3, 1.3, and $2.8(10^6)$ cm^{-3}, respectively.

on vibrational excitation of N_2 [*Richards et al.*, 1986; *Richards and Torr*, 1986a]. However, vibrationally excited N_2 was not included in the present investigation, noting that in a recent study of ionospheric behavior at Millstone Hill and Hobart during 1990, the FLIP model was able to reproduce the observed daytime densities extremely well without the need for an accounting of vibrationally-excited N_2 [*Richards et al.*, 1994a].

Most important reaction rates and cross sections that are used in the FLIP model are now reasonably well established [*Torr et al.*, 1990], and some innovative algorithms have been developed in recent years to incorporate actual measurements (e.g., F region heights or meridional winds) into the FLIP model when they are available [*Richards et al.*, 1995].

The FLIP model requires the following three key inputs: (1) the neutral atmosphere, (2) either the meridional component of the neutral wind or h_mF_2 (which is converted into a wind), (3) and the solar EUV flux. The neutral densities and temperatures are provided by the mass spectrometer and incoherent scatter (MSIS-86) model [*Hedin*, 1987]. Once the time and location of the required thermospheric parameters are specified, the only adjustable parameters in the MSIS model are the solar index (F10.7) and magnetic index (Ap). Both the solar activity and magnetic activity indices were stable in late March 1992. Under these circumstances, there was little day-to-day variation in the model calculation and it was possible to simulate just one day as being representative of the whole period, with no adjustments made to the input parameters to obtain better agreement with the data.

For this investigation the FLIP model winds were obtained

from the International Reference Ionosphere (IRI) model specifications for h_mF_2 during March 1992 using the servo-analysis method of *Richards* [1991]. For climatological studies, this method is preferred over using winds from the HWM90 model of *Hedin et al.* [1991] because the IRI h_mF_2 is based on a much larger database with greater global coverage.

For the EUV fluxes in FLIP we have used a new solar flux model called EUVAC [*Richards et al.*, 1994b] which is based on the F74113 solar EUV reference spectrum and the relative variations of the EUV flux observed by the Atmosphere Explorer E satellite. The EUVAC model produces 50-575 Å integrated fluxes that agree well with the most reliable rocket measurements.

Apart from the uncertainties in the neutral densities, winds, and EUV flux, there are uncertainties in the degree of particle and energy coupling between the ionosphere and plasmasphere. Although the FLIP model self-consistently includes coupling to the plasmasphere and the conjugate ionosphere, there can be large uncertainties in the plasma and heat content of the plasmasphere. There is currently no way of measuring or predicting the state of the plasmasphere as it recovers after magnetic storm depletions. These uncertainties in the plasmasphere have little effect on the daytime ionosphere, but there may be up to a factor of two difference in the calculated N_mF_2 (or equivalently a factor of 1.4 in the calculated f_0F_2) at night for extremes of assumptions about the plasmaspheric conditions. In this paper, the flux tubes were moderately depleted at the beginning of the run but filled up during the simulation periods. Thus flux tubes below L = 2, which fill up quickly, were close to full, while longer flux tubes were about half full during the simulation period.

The ionospheres in the auroral and equatorial regions are extremely difficult to model quantitatively with FLIP (and most other models). In the auroral zone there are electric fields, particle precipitation, and changes in neutral composition which are difficult to predict, while in the equatorial region the variation of the electric fields is the main cause of uncertainty. The FLIP model does not model the electron densities well in the equatorial and auroral zones primarily because it does not currently include convection electric fields. The model is now being modified to account for this.

2.2.3. The TIGCM. The NCAR TIGCM self-consistently calculates thermospheric and ionospheric structure, taking into account the dynamic coupling between the thermospheric neutral wind and the ionospheric plasma [*Roble et al.*, 1988]. It is an outgrowth of the NCAR Thermospheric General Circulation Model (TGCM) which included a non reactive empirical ionosphere and solved the primitive equations of dynamic meteorology adapted to the physics appropriate to thermospheric heights. The basic TGCM and associated developments have been described in detail by *Dickinson et al.* [1981, 1984], *Roble et al.* [1987], *Fesen et al.* [1986], and *Roble and Ridley* [1987].

The TIGCM employs an Eulerian approach to modeling the ionosphere as an alternative to the Lagrangian approach used by *Sojka and Schunk* [1985] and *Fuller-Rowell et al.* [1987]. Equations describing the ionosphere and thermosphere are both solved on the TGCM geographic grid and ion drift for the ionospheric calculation is obtained from the empirical model of *Richmond et al.* [1980] for low latitudes and mid latitudes while the empirical model of *Heelis et al.* [1982] or the Assimilative Mapping of Ionospheric Electrodynamics (AMIE) procedure [*Richmond*, 1992] is used for high latitudes. Therefore the model does not self-consistently solve for the naturally occurring electrodynamic coupling in the magnetospheric-ionospheric-thermospheric system. The TIGCM also employs a simple dipole magnetic field model with displaced geomagnetic and geographic poles. For inputs, the model requires specifications of several external sources. These include solar EUV and UV fluxes, auroral particle precipitation, the ionospheric convection pattern, and the amplitudes and phases of semi diurnal tides at the mesopause boundary.

The odd nitrogen chemistry is the same as that discussed by *Roble et al.* [1987]. $N(^2D)$ is assumed to be in photochemical equilibrium throughout the thermosphere and transport equations are solved for $N(^4S)$ and NO. The model considers $N(^4S)$ in photochemical equilibrium and specifies a constant number density of 8 x 10^6 cm^{-3} for NO at the lower boundary.

The ion-chemistry scheme, rate coefficients, and calculation procedure for the ionosphere can be reviewed in the works by *Roble et al.* [1987] and *Roble and Ridley* [1987], while the bulk motion includes both magnetic field-aligned diffusion and $\underline{E} \times \underline{B}$ forces in solving transport equations.

The upper boundary condition is diffusive equilibrium. The upper altitude limit of the model is about 550 km where an analytical formulation is used as a boundary condition for positive and negative flux transfer. This flux, which contributes to the overall density-height profile and equilibrium values of $f_0F_2(N_mF_2)$ and h_mF_2, results from normal topside dynamics (e.g., wind and electric field induced transport) as well as inputs from the conjugate ionosphere and fluxtube-coupled regions of the outer plasmasphere. Under equinox conditions with full fluxtubes, O^+ flows up from the ionosphere during the day, charge exchanges with neutral H to produce H^+, which in turn is stored in the outer plasmasphere. The process reverses at night, with the end result being an oversimplified diurnal characteristic which consists of an ebb and flow of plasma between the ionosphere and outer plasmasphere. This process is referred alternatively as plasmaspheric flux, magnetospheric flux, protonospheric flux, or ionospheric-plasmaspheric flux.

The lower boundary condition assumes photochemical equilibrium. Once the O^+ density distribution is defined, the NO^+, O_2^+, N_2^+ and N^+ distributions are determined by assuming photochemical equilibrium [*Roble and Ridley*, 1987]. The temperature, dynamics, composition, and the global ionosphere are calculated at each time step and the heating and cooling rates from chemical reactions, IR emissions, etc. are coupled into the thermodynamic equation at the next time step. Likewise, neutral winds, temperature, composition, and ionization rates are updated at each time step for the ionospheric calculation.

The TIGCM output provides global distributions of the neutral gas temperature and winds, ion drift velocities, the heights of constant pressure surfaces, and the number densities of O_2, N_2, O, $N(^2D)$, $N(^4S)$, NO, He, and Ar. It also solves for the ionospheric structure, giving global distributions of O^+, O_2^+, NO^+, N_2^+, N^+, electron density, and ion and electron temperatures. The TIGCM has an effective 5° latitude-longitude geographic grid with 25 constant pressure levels in the altitude range from approximately 97 km to 500 km. The time step can be flexible, varying from 3 min to 6 min, depending on the inputs. The model was exercised in a "weather" mode with an emphasis on March 28 and 29 in

IRI

TIGCM

FLIP

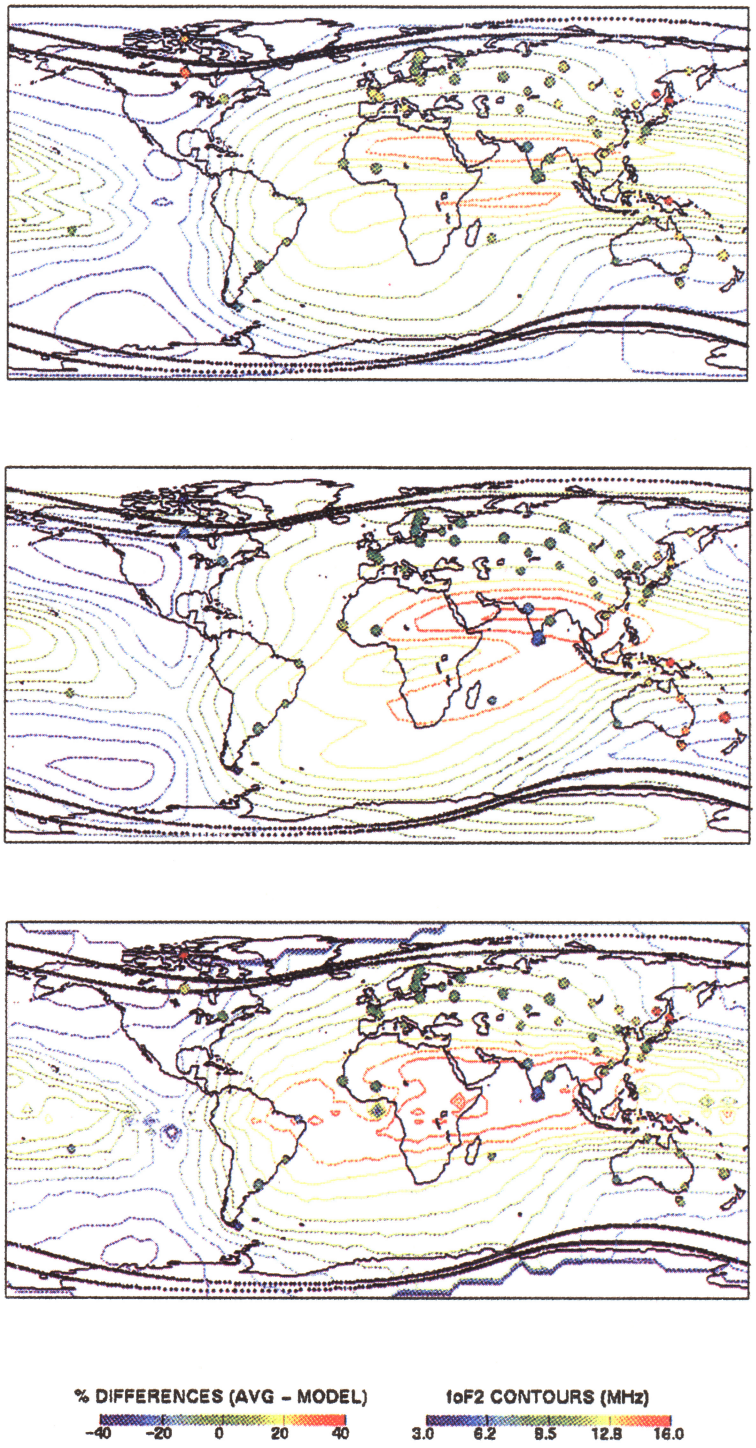

Plate 1. Global representation (1200 UT) of station locations and model-measurement comparisons of observed vs modeled values of f_0F_2. The color legend on the bottom left presents the percent differences between the data at each station (colored circles) and the IRI, the TIGCM and the FLIP model predictions in the top, middle, and bottom panels, respectively. See text for other details. Extrema on the f_0F_2 color scale (legend on bottom right side) for the isocontours are 3 and 16 MHz corresponding to extrema in N_mF_2 of 1.1(10^5) and 3.2(10^6) cm^{-3}, respectively. The red-to-blue color scale for the percent differences of model vs measurements covers the +40% to -40% range. (Note that differences of 20% and 40% in model-measurement comparisons of f_0F_2 are approximately equal to differences of 45% and 100%, respectively, in corresponding N_mF_2 comparisons.)

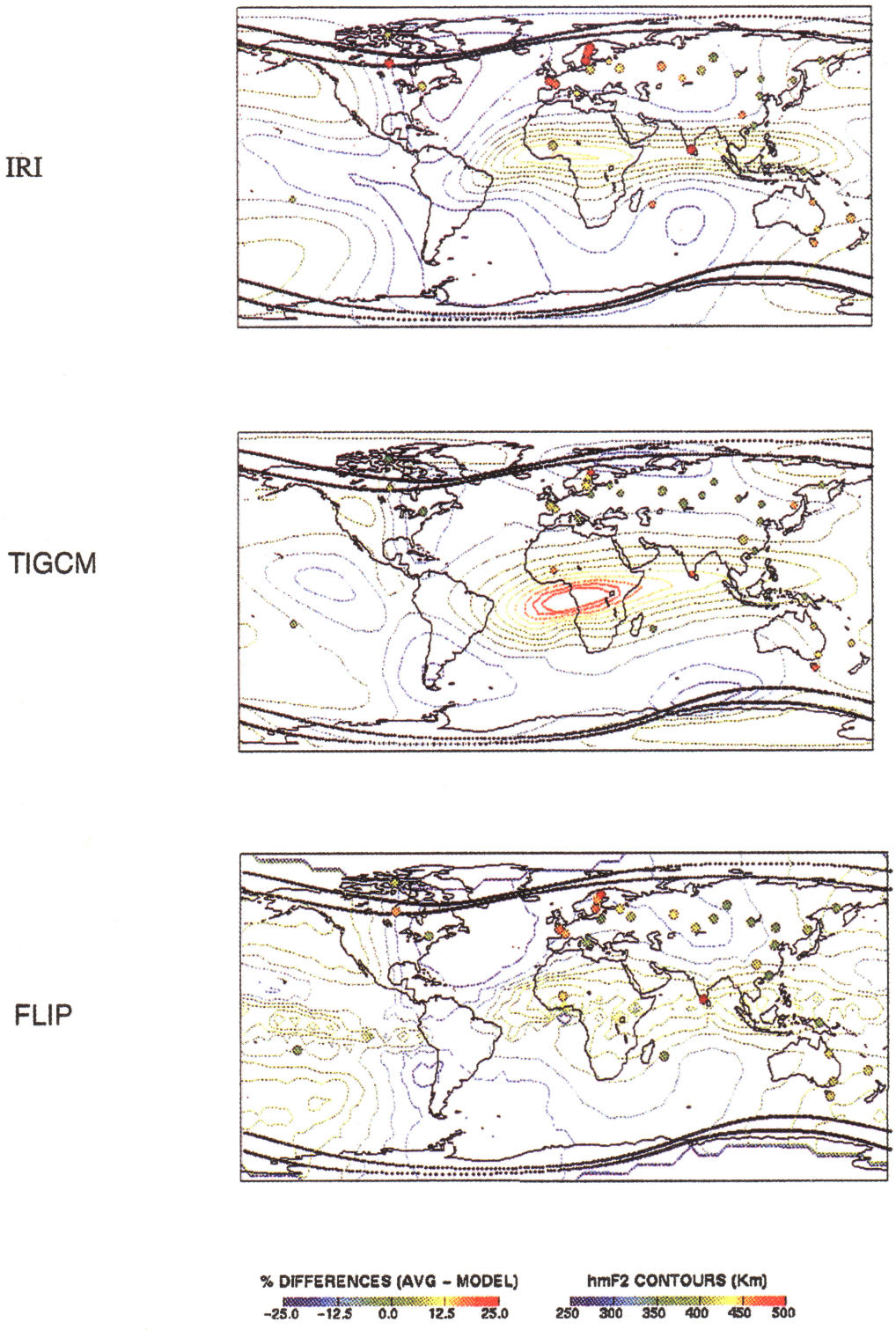

Plate 2. Global representation (1200 UT) of station locations and model-measurement comparisons of observed vs modeled values of h_mF_2. Color legend presents the percent differences between the data and the IRI, the TIGCM, and the FLIP model specifications in the top, middle, and bottom panels, respectively. See text for other details.

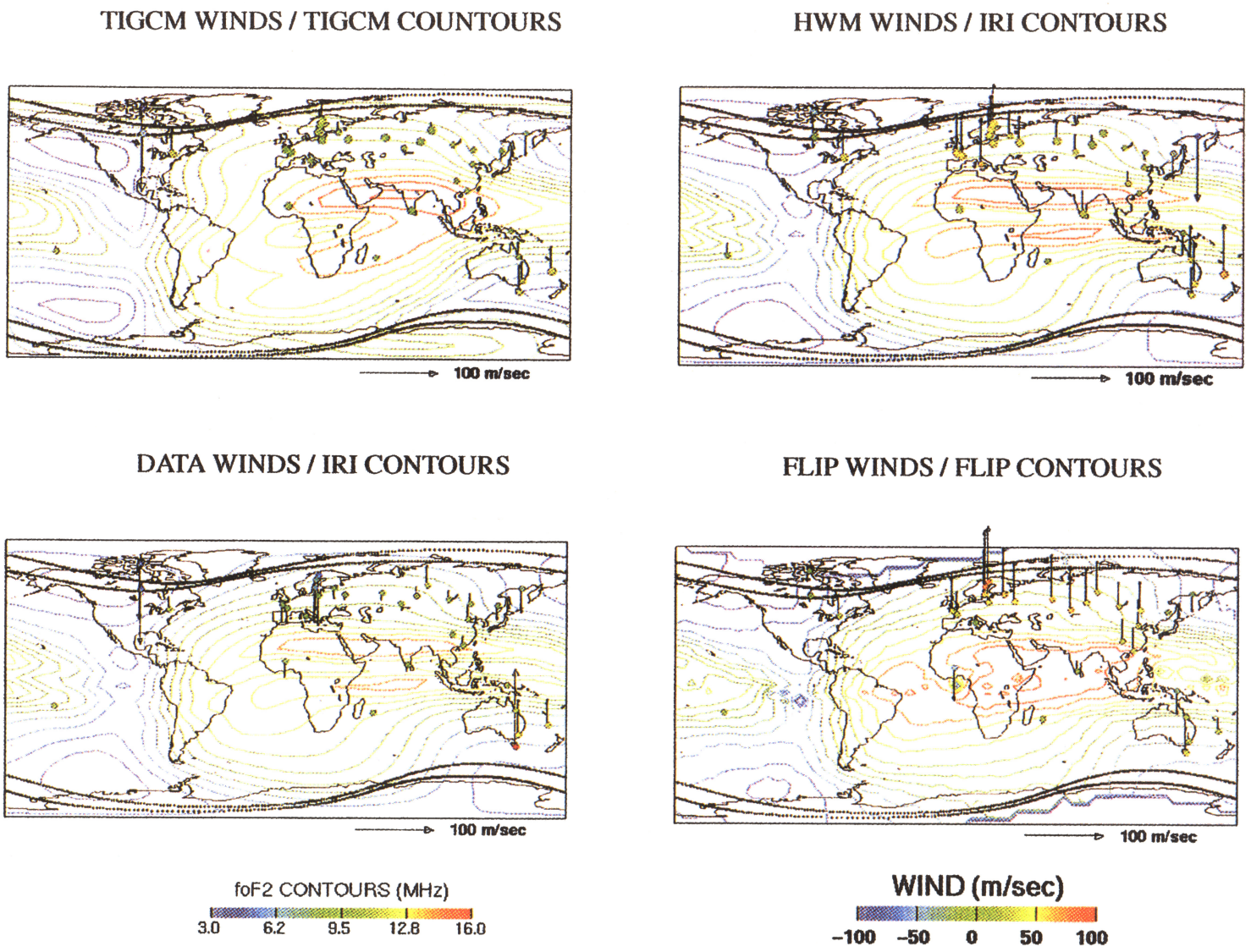

Plate 3. Global representation (1200 UT) of measured and modeled meridional winds at 300 km (for the models) and at h_mF_2 for the observations. Magnitude and directions are shown by vectors and color code at each of the station locations. Each panel is identified, and the f_0F_2 contours in the individual panels correspond to the model in question. In the data and HWM panels, the contours of f_0F_2 are from the IRI model.

studies of high-latitude electrodynamics [Lu et al., 1994; Emery et al., 1995]. It was also run in a "climatological" mode in order to specify the baseline conditions upon which to initiate the study of electrodynamics on the 28 and 29. The "climatological" run, described more fully by *Emery et al.* [this issue], is the basis for the TIGCM model-measurement comparisons carried out in this investigation.

For March 28 and 29 the average solar radiation index Sa (i.e., the 10.7 cm flux) was 188.5 x 10^{-22} W/m^2 Hz. This was the fundamental input driving the specification of the solar EUV and UV fluxes. For energetic inputs at high latitudes, ionospheric convection and particle precipitation were derived using the Assimilative Mapping of Ionospheric Electrodynamics (AMIE) procedure with approximately 50-min resolution; while low latitude and mid latitude ionospheric convection were derived from the empirical model of *Richmond et al.* [1980].

The semidiurnal tide model, described by *Fesen et al.* [1991], was included at the lower boundary of the TIGCM, and the model was first run to obtain a diurnally reproducible solution. For a "climatological" run, the patterns of the ionospheric convection and particle precipitation used in this investigation were an averaged AMIE prescription, derived from detailed data acquired during the 48-hour period March 28-29, 1992, and described in the companion paper by *Emery et al.* [this issue]. The time-dependent AMIE patterns were then incorporated into the TIGCM for a simulation of high-latitude thermospheric dynamics.

3. Model-Measurement Comparisons

3.1. Global Perspectives

Plates 1 and 2 provide global comparisons of the observed values of f_0F_2 and h_mF_2, respectively, at 1200 UT with the "predictions" of the IRI, the TIGCM, and the FLIP models (top, middle, and bottom panels, respectively). The observations at each station represent the value averaged over the campaign period for the UT (or LT) in question. The colored circles in the figures locate the stations, with the percent difference between the model predictions and the individual station observations defined by the color legend on the bottom left side of Plates 1 and 2. The bottom right-hand color bar defines the range of values for the color-coded isocontours in the plates (for f_0F_2 and h_mF_2 in Plates 1 and 2, respectively) which correspond to the outputs of each of the models in their respective panels. The abscissa is longitude with 0° at the center. The ordinate is latitude, extending north and south to ±90° from the geographic equator. The f_0F_2 contours are color-coded from a low value of 3 MHz (dark blue, N_mF_2 = 1.1(10)^5 cm^{-3}) to a high value of 16 MHz (red, N_mF_2 = 3.2 (10)^6 cm^{-3}). The h_mF_2 contours are also color-coded with a red-to-blue range extending from 500 to 250 km. The black curves at high northern/southern latitudes specify the boundaries of the auroral oval according to the Feldstein model for a moderate activity level Q = 4 [*Feldstein*, 1963; *Holtzworth and Meng*, 1975].

The f_0F_2 features (e.g., in the IRI panel) which dominate Plate 1 include (1) the sunrise terminator in the American sector rising in a span of approximately one hour from 5 to 10 MHz (i.e., N_mF_2 from 0.3 to 1.3 (10^6) cm^{-3}), and (2) the Appleton Anomaly with its peak densities somewhat symmetrically centered about the dip equator and extending in local time from 0900 to midnight. (The center of the plate corresponds to LT=1200 hours, while the left and right-hand edges correspond to LT=0 hours.) These large-scale features, along with the auroral oval boundaries, help identify important phenomenological domains while providing visual aides to the local time.

The f_0F_2 contours in Plate 1 show that the largest densities are at the daytime peaks of the Appleton Anomaly, with the highest value near 16 MHz (N_mF_2 = 3.2(10^6) cm^{-3}) at LT ≈ 1400 tapering off from the individual peaks to lower values equatorward and poleward. The lowest values are in the pre-dawn sector, with magnitudes near 5 MHz (N_mF_2 = 3(10)^5 cm^{-3}).

A review of the IRI panel in Plate 2 reveals maximum values of h_mF_2 at the daytime equator with magnitudes in the 425 km range. F region heights fall off poleward of the equatorial region and at all latitudes in evening and night time hours (LT ≥ 8 PM). Lowest F region heights are in the dawn sector at middle-to-high latitudes where values are near 275 km .

The FLIP and TIGCM panels in Plates 1 and 2 show characteristics similar to those described in the IRI panel with the exception that the FLIP model does not reproduce the well-known double peak of the Appleton Anomaly. This is primarily due to the fact that FLIP is designed for midlatitudes were it accounts for winds, chemistry, and plasmaspheric fluxes. It has no convection electric fields and therefore its results are compromised at low-to-equatorial latitudes where electric fields are important.

Each ionosonde site in Plates 1 and 2 is identified by a colored circle, with the color representing the percent difference between the observed value (f_0F_2 or h_mF_2) and the model prediction (i.e., percent difference = 100 (data - model)/data). The differences are presented on a scale of -40% to +40% in f_0F_2 and -25% to +25% in h_mF_2 (in both cases over the range blue to red as scaled in the legend).

We offer the following observations relative to Plate 1:

1. The IRI underestimates the values of f_0F_2, with the primary differences ranging from 0% (green) to 20% (yellow). There is no obvious LT dependence in the differences. Within a few percent this has been found to be true for all UT intervals.

2. Both the FLIP and TIGCM predictions demonstrate better agreement with the f_0F_2 data in daytime (more greens), and both depart in major ways from the data in the postsunset to presunrise period. In the nighttime hours the FLIP model and TIGCM tend to underestimate the critical frequencies of the F region peak by 20-40%. This is a consistent feature that prevailed for all UT intervals.

Reference to Plate 2 leads to the following observations regarding h_mF_2:

1. All three models either agree with the data (green) or underestimate the heights of the F region peaks by as much as 20 - 25% (orange to red).

2. The level of agreement between data and model are comparable for both the FLIP and TIGCM, whereas the overall results suggest that the IRI has the poorest representation of h_mF_2 among the three model comparisons displayed in Plate 2. This will be shown to be generally true but not by a large margin.

Before leaving the discussion of Plate 2 we note that the ionosonde values of h_mF_2 were derived from the $M(3000)F_2$ algorithm of *Dudeney* [1983]. Had we used the h_mF_2

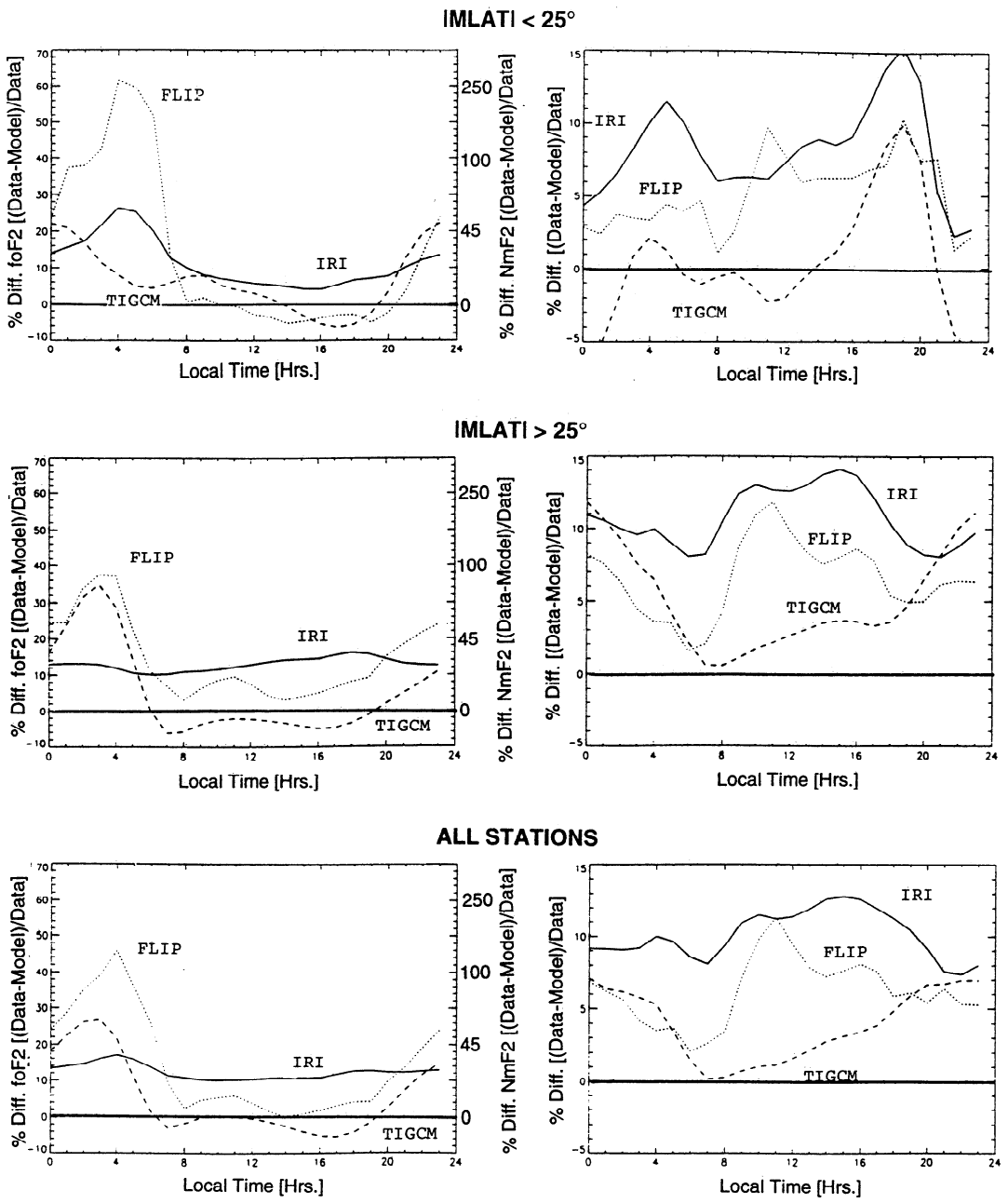

Figure 4. Integrated presentation of LT dependence of percent differences (ordinate) between the observations of f_0F_2 (left column) and h_mF_2 (right column) and the values from the IRI (solid curve), FLIP (dotted curve) and TIGCM (dashed curve) models. The right-hand axes of the f_0F_2 panels show the scaling for percent differences corresponding to N_mF_2 model-measurement comparisons. The bottom panels integrate the results of all stations, while the middle and upper panels restrict the comparisons to middle-to-high latitude stations (abs(MLAT) > 25°) and low-to-equatorial stations (abs(MLAT)< 25°), respectively.

formulism of *Bilitza et al.* [1979] instead, there would have been little-to-no difference at night and smaller ionosonde-derived values of h_mF_2 during the day. But the daytime difference between the Dudeney and Bilitza et al. approaches would generally be less than 2.5%.

3.2. An Integrated View of LT and Latitudinal Effects

Figure 4 provides an integrated view of the model-measurement comparisons with a perspective that establishes quantitative figures of merit for each of the models. The results in Figure 4 also help develop an understanding of inaccuracies in the model predictions that might be identified with geophysical domains or LT dependence.

The top, middle, and bottom panels present comparisons of the campaign-averaged data with the IRI, FLIP and TIGCM climatological "predictions" in regions for which abs(MLAT) < 25°, abs(MLAT) > 25°, and 0° ≤ abs(MLAT) ≤ 90°, respectively. The latter case involves all stations, while abs(MLAT) < 25° and >25° refer to model comparisons with the equatorial-to-low latitude and mid-to-high latitude

stations, respectively. The left column deals with f_0F_2 (with appropriate scaling for N_mF_2 along the right-side ordinate) and the right panel deals with h_mF_2. The abscissa is local time (LT), while the ordinate is the percent difference between the data and the model. (Positive values occur when the magnitudes of the observations are greater than the predictions of the model, that is, when the models underestimate the observable.) Each LT plot has been integrated over all universal times with a sliding 3 hour LT window for each UT from 0 through 23 hours.

Focusing first on the bottom panels of Figure 4 (comparisons with all stations) we offer the following conclusions:

1. The FLIP and TIGCM do very well in f_0F_2 (N_mF_2) daytime comparisons (6 < LT[hours] < 18), underestimating and overestimating the data by +3±3% (+6±6%) and -3±3% (-6±6%), respectively. (We note that positive percentages mean that the data values are in excess of the model values.) In the same LT period the IRI underestimates the data by +12±2% (+25±4%) with an overall diurnal characteristic that is virtually LT-independent.

2. The FLIP and TIGCM predictions for f_0F_2 (N_mF_2) show a marked departure from agreement with the observations in the post-sunset to pre-sunrise period (i.e., 18 ≤ LT ≤ 6), rising sharply from excellent agreement at sunset to disagreements at levels near 45% (110%) and 28% (64%) for the FLIP and TIGCM models, respectively, near LT = 4. An initial suggestion for the cause of this discrepancy is the "old unsolved problem" involving the maintenance of the nighttime ionosphere through plasmaspheric fluxes [see, e.g., *Evans*, 1975; *Sica et al.*, 1990]. We will discuss this issue more fully in subsequent sections, but first move on to other observations in Figure 4 including discrepancies in h_mF_2 and their associated impact on f_0F_2 values.

3. The bottom right panel in Figure 4 compares the observed values of h_mF_2 (all stations) with the model predictions. The results show that all models underestimate the observations by values less than 13%, with the IRI having the poorest and the TIGCM the best overall agreement with the data. In the postsunset to presunrise period the FLIP and TIGCM are nearly identical, generally underestimating h_mF_2 by 5±2%. At 300 km this is a 15 km underestimate, or equivalently a half scale height for N_2. If $O^+ + N_2 \rightarrow NO^+ + N$ and $NO^+ + e \rightarrow N + O$ were the primary loss channels for F peak densities, a theoretical underestimate in h_mF_2 by a half scale height in N_2 (i.e., 15 km) would account for a 50% increase in the loss rate of O^+ ions. This is indeed a potential contribution to the observed discrepancies in f_0F_2.

4. Continuing to review the results in the bottom-right panel of Figure 4, it can be seen that the FLIP and TIGCM models also underestimate the values of h_mF_2 during the daytime, with FLIP generally worse than the TIGCM. If all other physical processes in the two models were identical, one would expect (assuming the same principle loss mechanism discussed in item 3) that the FLIP model would predict lower values than the TIGCM for f_0F_2. On a relative scale this is consistent with the daytime findings in the bottom left panel of Figure 4 where FLIP underestimates and the TIGCM overestimates the values of f_0F_2.

5. Turning attention to the middle and upper panels of Figure 4, it can be seen that the post-sunset to pre-sunrise discrepancy in f_0F_2 exists at middle-to-high and low-to-equatorial latitudes, respectively. This would suggest that downward transport of H^+ at night and subsequent charge exchange with O to form increased levels of O^+ is not the cause for the f_0F_2 model-measurement discrepancy. This is because such downward plasmaspheric transport of H^+ is effectively zero at low-to-equatorial latitudes. This interpretation of results is not without counter and supporting arguments. Note for example that the pre-sunrise TIGCM results for f_0F_2 are generally better at low latitudes than at mid-to-high latitudes, suggesting that flux is at least part of the problem. And while the FLIP results at night are worse at low-to-equatorial latitudes, the model includes no electric fields which have a dominant control of heights and densities at equatorial latitudes. At night these electric field controls tend to move h_mF_2 to lower altitudes, thus reducing the plasma densities below those currently predicted by the FLIP model. This suggests that the problem is neither electric fields nor plasmaspheric fluxes.

6. Final observations in Figure 4 focus on h_mF_2, where the equatorial-to-low latitude results (top right panel) are uniquely different from those at mid-to-high latitudes. The primary difference is at post-sunset and to a lesser degree at presunrise. The postsunset discrepancy is most likely the result of the well-know postsunset prereversal enhancement in F region heights at equatorial latitudes. This is a dynamo effect, not included in the simple electric field model of *Richmond et al.* [1980] that is employed in the TIGCM. It is interesting to note that it is also not accounted for in the empirically based IRI, suggesting too little data during that period of the day or too much smoothing of the results. The presunrise enhancement, if we allow ourselves to call it that, is a new observation, with causality most likely associated with ionospheric expansion due to heating at F region sunrise. This issue will be taken up again in section 3.4.

3.3. Effects of Thermospheric Winds

The results in Figure 4 suggest a consistency between the f_0F_2 and h_mF_2 observations, in that model underestimates of f_0F_2 were correlated with underestimates of h_mF_2. And this correlation was supported by simple arguments of recombination chemistry. In this section, further analysis of the data allows causality to be traced to model representations

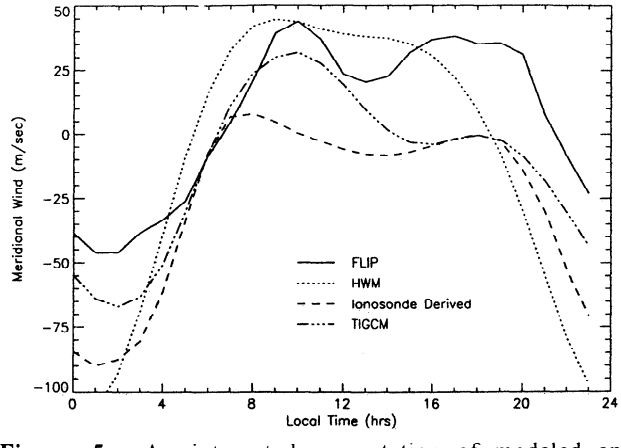

Figure 5. An integrated presentation of modeled and measured meridional winds over all stations for which 20° < abs(MLAT) < 60°. Positive values are poleward, while negative values are equatorward.

of meridional winds, known to have strong influences on h_mF_2 at mid latitudes.

Plate 3 presents a global perspective of magnetic meridional winds as predicted by the TIGCM, the empirically-based Horizontal Wind Model (HWM) [Hedin, 1991], and the FLIP model. Plate 3 also includes the magnetic meridional winds measured by the SUNDIAL network of ionosondes using the h_mF_2 servo-analysis procedures of *Miller et al.* [1993; and "A fast method for the derivation of meridional winds from the height of the ionospheric F_2 region," submitted to *J. Geophys. Res.*, 1995] with the *Dudeney* [1983] formulation for h_mF_2. (With regard to the accuracy of this h_mF_2 servo-analysis procedure we note that several comparisons have been made of winds derived from h_mF_2 with meridional winds derived from other methods. These have been primarily with incoherent scatter radars [see, e.g., *Ilgi et al.*, 1995], although *Miller et al.* [1986] and Miller [1989] also compared results with winds measured by Fabry-Perot interferometry. In each of these comparisons the winds derived from h_mF_2 measurements were found to be consistent with the results of the other techniques, both in magnitude and in the pattern of variability.) This h_mF_2 servo-analysis technique was applied to all ionosonde stations regardless of latitude, but with the caveat that the results are not expected to be realistic representations of meridional winds in regions for which abs(MLAT) < 20°.

The presentation of meridional winds in Plate 3 is at UT = 12 with f_0F_2 contours and auroral oval boundaries as previously described. Wind magnitudes are depicted by scaled vector lengths and by color codes at each of the stations. Plate 3 is useful in so far as it develops an appreciation for station distributions and general perspectives on variations with latitude and local time. A review of Plate 3 shows marked differences between and among the findings of the TIGCM, the HWM, and the FLIP predictions, with the TIGCM appearing to be in best agreement with the ionosonde-derived winds. This is in fact consistent with a general finding when a plot showing LT-dependence (integrated over all UTs) is developed for detailed comparisons between measured and modeled winds. Such a comparison is presented in Figure 5 where the abscissa is LT and the ordinate is the magnitude of meridional winds predicted by each of the models or measured by the ground-based network of ionosondes. Only stations in the region 20° < abs(MLAT) < 60° were considered in this comparison since this is the general bound of applicability of the servo-analysis technique. Positive winds are poleward, while negative winds are equatorward.

Review of Figure 5 leads to the following observations:

1. There is a large spread in values in both daytime and nighttime sectors. The daytime spread is 0 to 40 m/s, while the nighttime spread is 30 to 90 m/s.

2. The model in best agreement with the data is the TIGCM.

3. At night the FLIP and TIGCM winds are both less than the observations, suggesting that their values of h_mF_2 should be less than those observed. This is consistent with the findings in Figure 4 as well as with the argument that weaker equatorward winds result in lower values of h_mF_2. Hence we have established (at least in part) model underestimates of nighttime meridional winds as the cause for lower nighttime model predictions of h_mF_2 and f_0F_2 (i.e., N_mF_2).

4. During the day the observations show very light winds, generally ±10 m/s, whereas FLIP and HWM are typically in the 25 m/s range. Both FLIP and the TIGCM predict stronger daytime winds than those observed. FLIP winds are stronger than those of the TIGCM suggesting lower values of h_mF_2 than those predicted by TIGCM. This is consistent with the comparisons discussed in Figure 4.

In closing the discussion of Figure 5 we note that the low ionosonde values for daytime winds are corroborated by the mid-latitude observations of *Ilgi et al.* [1995] during summer and equinox periods using both ionosonde and MU radar techniques. This corroboration, taken in concert with the global observations presented here and associated model comparisons, suggests that current wind models must be more carefully evaluated not only under nighttime conditions (as discussed above in connection with maintenance of the nighttime ionosphere) but in the daytime as well.

3.4 Modeling the Plasmaspheric Flux.

The previous sections have established a cause-effect path which links model underestimates in nighttime values of f_0F_2 to underestimates in h_mF_2 and finally to underestimates in the meridional component of the prevailing thermospheric winds. Ancillary arguments have also suggested that the nighttime discrepancy in f_0F_2 might be due in part to inaccurate model specification of plasmaspheric fluxes.

The issue of plasmaspheric fluxes and their contribution to the maintenance of the nighttime ionosphere has itself been somewhat of a controversy without definitive resolution. Part of the problem is the difficulty in the measurement itself. The early work of *Evans* [1975] suggested that the incoherent scatter radar technique was perhaps the best approach, but even it, according to Evans, has difficulty in uniquely and quantitatively determining the flux. Among the difficulties is the signal-to-noise ratio at night and the need to eliminate layer dynamics (i.e., induced by winds and electric fields) in order to determine the true plasmaspheric contributions. In his study of five nights (near local midnight at Millstone Hill) spanning four seasons, he found average fluxes at $3(10)^7/cm^2$ s. He also found that H^+ was a minor ion (never greater than 25%) over the altitude range over which useful measurements were made (i.e., < 800 km), and that the majority of the results exhibited a decrease in the O^+ flux with altitude. This altitude dependence indicated that the layers were descending and corrections had to be made. The maximum flux values were at or near h_mF_2 and approached $2(10)^9/cm^2$ s, a value clearly dominated by topside layer dynamics. In the end he concluded that large increases in plasmaspheric fluxes, that could give rise to nighttime increases in total electron content, did not appear to be seen. This conclusion was in keeping with that of *Jain and Williams* [1974]. We pursue this issue further with a discussion of these fluxes as specified within the TIGCM and the FLIP models.

The TIGCM invokes a sinusoidal latitudinal variation of this flux in which it is defined as zero at the magnetic equator and constant above 60° mlat. The flux model is discontinuous at 60°, with day/night values just equatorward set at $+2(10)^8/-2(10)^8$ cm^2 s, and values of $3(10)^8/-1(10)^8$ cm^2 s just poleward of that. The region above 60° is constant in latitude, while below 60° it goes to zero at the magnetic equator in a cosine fashion. There is no LT dependence in the flux model with the exception of an interpolation routine from the day/night levels between zenith angles of 80° and 110°. We note that the TIGCM includes no H^+ transport or

associated charge-exchange chemistry. This flux model is applied at the upper altitude limit of the TIGCM (approximately 550 km) and is intended to include all effects on O^+ (i.e., topside layer dynamics and protonospheric fluxes).

By contrast, the FLIP model approaches the plasmaspheric flux issue self-consistently along fluxtubes from hemisphere to hemisphere. It has already been pointed out that uncertainties in the fluxes between the ionosphere and the plasmasphere have little effect on the daytime ionosphere, but there may be up to a factor of two difference in the calculated N_mF_2 densities (or equivalently a factor of 1.4 in the calculated values of f_0F_2) at night for extremes in assumptions about the plasmaspheric conditions. In this work, the fluxtubes in the FLIP simulations were moderately depleted at the beginning of the run but filled up after several cycles of the simulation. The expectation therefore is that maximum plasmaspheric flux is already making its contribution to the nighttime FLIP values of f_0F_2.

Figure 6 plots the flux levels derived in the FLIP model in the 20° meridian for 30°, 50°, and 70° northern geographic latitudes at the 550-km level. These fluxes represent values that integrate the effects on O^+ of layer movement due to winds and electric fields, photoproduction (in the daytime), heating and cooling of the plasma, and ionospheric-plasmaspheric exchange. The 550 km height is the approximate topside boundary for the TIGCM and has been selected for comparison with its analytical flux formulation.

The interpretation of the fluxes in Figure 6 is complicated by the fact that 550 km is in an altitude regime where measurements by *Evans* [1975] have indicated that the daytime flux changes sign from downwards at lower altitudes to upwards at higher altitudes. Below this "transition" level, excess ions flow down under the influence of gravity to regions of higher loss in reactions with N_2 and O_2, while above this altitude O^+ ions flow upwards, and through charge exchange with H, produce H^+ ions. Some of the flux variation in Figure 6 is due to movement of the altitude of the transition between upward and downward flux. Figure 6 shows that there are three prominent features of the diurnal flux variation: the sunrise and midday upward flux maxima,

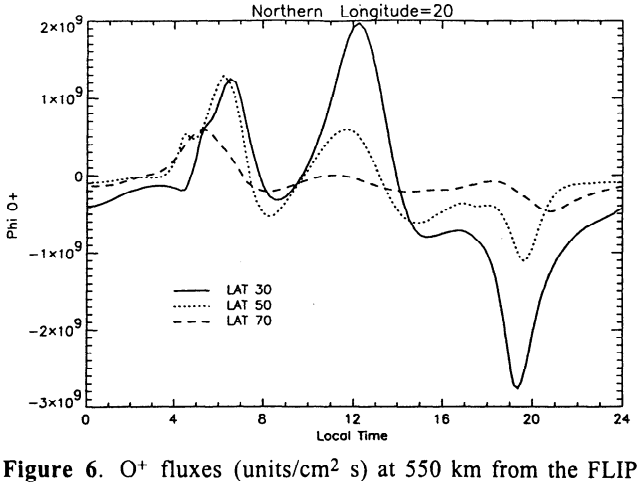

Figure 6. O^+ fluxes (units/cm^2 s) at 550 km from the FLIP model in the 20° E meridian at 30°N (solid curve), 50°N (dotted curve), and 70°N (dashed curve) geographic latitude.

and the postsunset downward flux maximum. (The southern hemisphere O^+ flux variation shows similar features to the northern hemisphere variation discussed here.) The sunrise peak in the O^+ flux is principally a consequence of the thermal expansion of the ionospheric plasma. The low density in the morning allows the electron temperature to rise steeply, causing a large increase in scale height that is seen as a large flux in the topside ionosphere [*Richards and Torr*, 1986]. Because of the tilt of the magnetic field, the sun rises more than half an hour earlier in the southern hemisphere than in the northern hemisphere and this causes predawn heating which leads to the initial upward surge in flux. From the point of view of photoelectron heating, sunrise occurs at about 100° solar zenith angle compared to about 90° for photoionization. The upward flux receives an additional boost at local sunrise. The separation of the two sunrises produces an inflection on the flux curves for 30°N and 50°N geographic latitudes. The sunrise effect is not as dramatic at 70°N because the changes in electron temperature are likewise not as dramatic. Heat from the plasmasphere keeps the ionospheric electron temperature high at night.

After the sunrise increase in flux there is an abatement until mid morning due to a decrease in the electron temperature as the plasma density builds up and also because of a poleward wind which pushes ions down the field lines.

The flux increases after the morning low as a result of an abatement of the poleward wind and the substantial photoproduction of ions which peaks near noon. The decrease in the magnitude of the midday O^+ upward flux with increasing latitude is partially due to the lowering of the layer as a result of a latitudinal increase in the poleward wind. The daytime upward O^+ fluxes at 50 degrees latitude are comparable to the fluxes observed by *Evans* [1975].

The large downward flux after sunset is caused by the thermal collapse of the ionosphere. This collapse is exaggerated by the fact that the electron cooling is large because plasma density remains high while the heating is shut off. The effect decreases with latitude because the plasmaspheric heat reservoir reduces the severity of the thermal collapse. In addition, larger equatorward winds help to keep the ionization higher at high latitudes.

The flux characteristics in Figure 6 are clearly not like those in the analytical formulation of the TIGCM. For immediate purposes, however, we focus on the postmidnight to presunrise period where we have documented the discrepancy between observed and modeled values of f_0F_2 and where we seek to confirm or deny plasmaspheric flux as a causality. Remembering the cosine characterization of nighttime flux in the TIGCM with a maximum downward value of -2(10^8) cm^2 s at 60° MLAT, we focus on the FLIP values at 50°N ($\approx$50 MLAT at 20° E longitude). Those values vary from -1.5(10^8) cm^2 s at LT=0 to zero at LT=4. If the FLIP results were to be the guide, and consistency with the observations of *Evans* [1975] an empirical boundary, we conclude the following: (1) that the filled-fluxtube fluxes of FLIP represent a maximized "saturated" plasmaspheric input to the postmidnight ionosphere, (2) the TIGCM fluxes, while requiring a more realistic LT and latitudinal dependence, need not have fluxes increased in the post-midnight period, and (3) that thermospheric winds, not plasmaspheric flux, is the primary cause for FLIP and TIGCM model underestimates of the densities and heights of the nighttime F region.

Table 2. Summary of Nominal Percent Differences in N_mF_2 Model-Measurement Comparisons (Positive/Negative Percentages Represent Model Under/Over Specifications of N_mF_2 Values.)

	Daytime (6≤LT≤18)			Postmidnight (0≤LT≤5)		
Model	|MLAT|<25°	|MLAT|>25°	All	|MLAT|<25°	|MLAT|>25°	All
IRI	28±10%	+28±6%	+25±4%	+44±12%	+23±2%	+32±4%
FLIP	0(+96/-17%)	+12±6%	+6±6%	+119±28%	+69±17%	+82±21%
TIGCM	0±17%	-8±4%	-6±6%	+39±8%	+56±21%	+39±17%

4. Comments and Conclusions

The overall comparison between the data and the models suggests that the physics of the daytime F region climatology is reasonably well understood. This is based on the March-April 1992 period of the SUNDIAL/ATLAS 1 campaign and the accuracies between the f_0F_2 (i.e., N_mF_2) predictions of the IRI, the FLIP and the TIGCM models, and the database of 53 ionosondes. Reference to Table 2 shows that the IRI, FLIP and TIGCM model specifications of daytime N_mF_2 values (6≤LT≤18) agree with the full complement of stations within accuracies of 25±4%, +6±6%, and -6±6% respectively, with variations in these percentages when the comparisons are restricted to equatorial-to-low latitudes (i.e., abs(MLAT) < 25°) and middle-to-high latitudes (i.e., abs(MLAT) > 25°).

There is a marked difference in the accuracies in the postsunset to presunrise period, with the maximum disagreements occurring in the postmidnight period at about 0400 LT. Defining this postmidnight period as LT = 0 to 5 hours, Table 2 shows that the inaccuracy in FLIP and the TIGCM specifications for N_mF_2 can be 82±21% and 39±17% , respectively, when the results are integrated over all stations. These results, in effect, rediscovered the old but unsettled issue of our understanding of the maintenance of the nighttime ionosphere and quantified it in terms of relative and absolute accuracies among the three models and the observations.

Recently, *Sica et al* [1990] have drawn some attention to this problem in their inabilities to uniquely differentiate the relative influences of meridional winds and protonospheric fluxes on modeled values of N_mF_2 and h_mF_2. They pointed out that any number of reasonable but nonunique admixtures of meridional wind speeds and protonospheric fluxes could give rise to identical values of N_mF_2. Their database was only that of a network of f_0F_2 measurements from midlatitude ionosondes.

Pursuing the issue further in this investigation, correlations were carried out that involved measurements of f_0F_2 (N_mF_2), h_mF_2, and meridional winds. And these correlations were integrated over all stations as well as over stations restricted to equatorial-to-low and mid-to-high latitudes. The correlations also involved considerations of the physical assumptions within the FLIP and TIGCM models, wherein FLIP self-consistently solves for the plasmaspheric flux inputs while the TIGCM invokes a relatively simple analytical formalism. The correlations showed a cause-effect chain in which the low model values of f_0F_2 were traceable to low model values for h_mF_2 (and associated increases in recombination losses) and ultimately to low model values of nighttime meridional winds. The search for causality identified with nighttime protonospheric fluxes tended to suggest that they were of secondary concern. This was shown to be particularly true since the self-consistent solution of FLIP flux values was in general agreement with those in the post-midnight TIGCM flux formalism.

No consideration was given to electric field effects, where at least at mid-latitudes their influences are expected to be minimal. Nor was there any attention given to thermospheric densities and composition. It is possible that thermospheric densities and composition played a role in the discrepancies, but the relatively good agreement between the models and the data in the daytime suggested some confidence in the individual model treatments of thermospheric densities and composition.

Current efforts are focusing on the addition of convection electric field formalisms to the FLIP and an improved representation of topside fluxes into the TIGCM. The intent is to include local time and latitudinal controls. This will represent a convergence of predictive methodologies and a closer scrutiny of cause-effect relationships.

Acknowledgments. The authors wish to thank the institutions and agencies in each of the countries which participated in this investigation. The overall effort was supported by the Space Physics Division of the National Aeronautics and Space Administration under contract NASW-4755.

The Editor thanks D. Bilitza and another referee for their assistance in evaluating this paper.

References

Abdu, M.A., J.A.H. Sobral, P. Richards, M.M. deGonzalez, Y.N. Huang, B.M. Reddy, K. Cheng, E.P. Szuszczewicz, and I.S. Batista, Zonal/meridonal winds and disturbance dynamo electric field control of the low-latitude ionosphere based on the SUNDIAL/ATLAS 1 campaign, J. Geophys. Res. [this issue].

Bilitza, D., Topside models: Status and future improvements, Adv. Space Res., 14 (12), 17, 1994.

Bilitza, D., R. Eyfrig, N.M. Sheikh, A global model for the height of the F2-peak using M3000 values from the CCIR numerical map, ITU Telecomm. J., 46, 549, 1979.

Bilitza, D., K. Rawer, L. Bossy, and T. Gulyaeva, International reference ionosphere - Past, present and future, II., Plasma temperatures, ion composition and ion drift, Adv. Space Res., 13 (3), 15, 1992a.

Bilitza, D., K. Rawer, L. Bossy, and T. Gulyaeva, International reference ionosphere - past, present, and future: I. Electron density, Adv. Space Res., 13 (3) 3, 1992b.

Broadfoot, A.L., B.R. Sandel, D.J. Knecht, R.R. Viereck and E. Murad, Panchromatic spectrograph with supporting monochromatic imagers, Appl. Opt., 31, 3083, 1992.

Dickinson, R.E., E.C. Ridley, and R.G. Roble, A three-dimensional, time-

dependent general circulation model of the thermosphere, J. Geophys. Res., 86, 1499, 1981.

Dickinson, R.E., E.C. Ridley, and R. G. Roble, Thermospheric general circulation with coupled dynamics and composition, J. Atmos. Sci., 41, 205, 1984.

Dudeney, J.R., The accuracy of simple methods for determining the height of the maximum electron concentration of the *F*2-layer from scaled ionospheric characteristics, J. Atmos. Terr. Phys., 45, 629, 1983.

Emery, B., et al., AMIE in the TIGCM comparisons with global Ionospheric and thermospheric observations during the GEM/SUNDIAL period of March 28-29, 1992, J. Geophys. Res., this issue.

Evans, J.V., A study of *F*2 region night-time vertical ionization fluxes at Millstone Hill, Planet. Space Sci, 23, 1611, 1975.

Fejer, B.G., R.W. Spiro, R.A. Wolf, and J.C. Foster, Latitudinal variation of perturbation electric fields during magnetically disturbed periods: 1986 SUNDIAL observations and model results, Ann. Geophys., 8, 441, 1990.

Feldstein, Y.I., On morphology of auroral and magnetic disturbances at high latitudes, Geomagn. Aeron., 3, 183, 1963.

Fennelly, J.A., D.G. Torr, P.G. Richards, and M.R. Torr, Simultaneous retrieval of the solar EUV flux and neutral thermospheric O, O_2, N_2 and temperature from twilight airglow, J. Geophys. Res., 99, 6483, 1994.

Fesen, C.G., R.E. Dickinson, and R.G. Roble, Simulation of thermospheric tides at equinox with the National Center for Atmospheric Research thermospheric general circulation model, J. Geophys. Res., 91, 4471, 1986.

Fesen, C.G., R.G. Roble, and E.C. Ridley, Thermospheric tides at equinox: Simulation with coupled composition and auroral forcings, 2. Semidiurnal component, J. Geophys. Res., 96, 3663, 1991.

Foster, J.C., J.M. Holt, R.G. Musgrove, and D.S. Evans, Ionospheric convection associated with discrete levels of particle precipitation, Geophys. Res. Lett., 13, 656, 1986.

Fuller-Rowell, T.J., et al., Interactions between neutral thermospheric composition and the polar ionosphere using a coupled ionosphere-thermosphere model, J. Geophys. Res., 92, 7744-7748, 1987.

Gardner, J.A., R.A. Viereck, E. Murad, D.J. Knecht, C.P. Pike, A.L. Broadfoot, and E.R. Anderson, Simultaneous observations of neutral and ionic magnesium in the thermosphere, Geophys. Res. Lett., 22, 2119, 1995.

Hedin, A.E., MSIS-86 thermosphere model, J. Geophys. Res., 92, 4649, 1987.

Hedin, A.E., et al., Revised global model of thermospheric winds using satellite and ground-based observations, J. Geophys. Res., 96, 7657, 1991.

Heelis, R.A., J.K. Lowell, and R.W. Spiro, A model of the high-latitude ionospheric convection pattern, J. Geophys. Res., 87, 6339-6345, 1982.

Holtzworth, R.H., and C.I. Meng, Mathematical representation of the auroral oval, Geophys. Res. Lett., 2, 337, 1975.

Ilgi, S., W.L. Oliver, T. Ogawa, and S. Fukao, Thermospheric winds over Japan: Comparison of ionosonde and radar measurements, J. Geophys. Res, 100, 21323-21328, 1995.

Jain, A.R. and P.J.S. Williams, Vertical transport of plasma in the night-time ionosphere, J. Atmos. Terr. Phys. 36, 417, 1974

Kamide, Y., Problems in studies of magnetic storms: An introductory remark, in Proceedings of the International Conference on Magnetic Storms, pp. 1-9, Nagoya Univ. Press, Hohkaido, Japan, 1994.

Lester, M., J.A. Davies, H. Luhr, and T.S. Virdi, High-latitude Hall and Pedersen conductances during substorm activity in the SUNDIAL/ATLAS campaign, J. Geophys. Res., this issue.

Lu, G., A.D. Richmond, B.A. Emery, and R.G. Roble, Magnetosphere-ionosphere-thermosphere coupling: Effect of neutral winds on energy transfer and field aligned current, J. Geophys. Res., 100, 19,643, 1995.

Lu, G., et al., High-latitude ionospheric electrodynamics as determined by the AMIE procedure for the conjunctive SUNDIAL/ATLAS 1/GEM period, J. Geophys. Res., this issue.

Luhr, H., S. Thuurey, and N. Klocker, The EISCAT magnetometer cross. Operational aspects - First results, Geophys. Surv., 6, 305, 1984.

Miller, K.L., P.G. Richards, and H.Y. Wu, A global-study of meridional winds and electron densities in the *F* region during the SUNDIAL 1987 campaign, Ann. Geophys., 11, 572, 1993.

Miller, K.L., D.G. Torr, and P.G. Richards, Meridional winds in the thermosphere derived from measurements of *F*2 layer height, J. Geophys. Res., 91, 4531, 1986.

Miller, K. L., P. Richards, and D. G. Torr, The derivation of meridional neutral winds in the thermosphere from F2 layer height, in World Ionosphere/Thermosphere Study, WITS Handbook, vol. 2, edited by C. H. Liu, pp. 439-471, SCOSTEP Secretariat, University of Illinois, Urbana, Ill., 1989.

Nagy, A.F., and P.M. Banks, Photoelectron fluxes in the ionosphere, J. Geophys., 75, 6269, 1970.

Pulinets, S., D. Evans, and M. Lester, UT and LT variations in the development of ionospheric disturbances over Russian longitudes, J. Geophys. Res., this issue.

Rawer, K., "International reference Ionosphere - IRI 79, NOAA Rep., UAG-82, U.S. Dep. of Comm., Washington, D. C., 1981.

Rawer, K., and Y.V. Ramanamurty, International Reference Ionosphere-Status 1985/1986, Adv. Space Res. 5 (10), 1985.

Richards, P.G., An improved algorithm for determining neutral winds from the height of the F_2 peak electron density, J. Geophys. Res., 96, 17,839, 1991.

Richards, P.G., and D.G. Torr, A factor of 2 reduction in the theoretical *F*2 peak electron density due to enhanced vibrational excitation of N_2 in summer at solar maximum, J. Geophys. Res., 91, 11,331, 1986a.

Richards, P., and D. Torr, Thermal coupling of conjugate ionospheres and the tilt of the Earth's magnetic field, J. Geophys. Res., 91, 9017, 1986b.

Richards, P.G., and D.G. Torr, Ratios of photoelectron to EUV ionization rates for aeronomic studies, J. Geophys. Res., 93, 4060, 1988.

Richards, P.G., D.G. Torr, and W.A. Abdon, Effects of vibrational enhancement of N_2 on the cooling rate of ionospheric thermal electrons, J. Geophys. Res., 91, 304, 1986.

Richards, P.G., D.G. Torr, B.W. Reinisch, R.R. Gamache, and P.J. Wilkinson, F_2 peak electron density at Millstone Hill and Hobart: Comparison of theory and measurement at solar maximum, J. Geophys. Res., 99, 15,005, 1994a.

Richards, P.G., J.A. Fennelly, and D.G. Torr, EUVAC: A solar EUV flux model for aeronomic calculations, J. Geophys. Res., 99, 8981, 1994b.

Richards, P.G., M.P. Hickey, and D.G. Torr, New sources for the hot oxygen geocorona, Geophys. Res. Lett., 21, 657, 1994c.

Richards, P.G., D.G. Torr, M.E. Hagan, and M.J. Buonsanto, A new algorithm for improved ionospheric electron density modeling, Geophys. Res. Lett., 22, 1385, 1995.

Richmond, A.D., Assimilative mapping of ionospheric electrodynamics, Adv. Space Res., 12 (6), 59, 1992.

Richmond, A.D., and Y. Kamide, Mapping electrodynamic features of the high-latitude ionosphere from localized observations: Combined incoherent scatter radar and magnetometer measurements for Jan 18-19, 1984, J. Geophys. Res., 93, 5741, 1988.

Richmond, A.D., et al., An empirical model of quiet-day ionospheric electric fields at middle and low latitudes, J. Geophys. Res., 85, 4658-4664, 1980.

Roble, R.G., and E.C. Ridley, An auroral model for the NCAR thermospheric general circulation model (TGCM), Ann. Geophys., Ser.A, 5(6), 369, 1987.

Roble, R.G., E.C. Ridley, and R.E. Dickinson, On the global mean structure of the thermosphere, J. Geophys. Res., 92, 8745-8758, 1987.

Roble, R.G., E.C. Ridley, A.D. Richmond, and R.E. Dickinson, A coupled thermosphere/ionosphere general circulation model, Geophys. Res. Lett., 15, 1325, 1988.

Schunk, R.W., and A.F. Nagy, Electron temperatures in the F region of the ionosphere: Theory and observations, Rev. Geophys., 16, 355, 1978.

Schunk, R.W., and E. P. Szuszczewicz, First principle and empirical modeling of the global-scale ionosphere, Ann. Geophys., 6, 19, 1988.

Sica, R., R.W. Schunk, and P. Wilkinson, A study of the undisturbed mid-latitude ionosphere using simultaneous, multiple-site ionosonde measurements using the SUNDIAL '86 campaign, J. Geophys. Res., 95, 8727, 1990.

Sime, D., and R. Behnke, The U.S. space weather program, 1, STEP Int., 4, (No. 11), Nov. 1994.

Siscoe, G., E. Hildner, T.H. Killeen, L.J. Lanzerotti, and W. Lotko, Developing service promises accurate space weather forecasts in the future, Eos, Trans. Am. Geophys. Union, 75, 353, 1994.

Sojka, J.J., and R.W. Schunk, A theoretical study of the global *F* region for June solstice, solar maximum, and low magnetic activity, J. Geophys. Res., 90, 5285, 1985.

Spiro, R.W., R.A. Wolf, and B.G. Fejer, Penetration of high-latitude-electric-field effects to low latitudes during SUNDIAL 1984, Ann. Geophys., 6, 39, 1988.

Szuszczewicz, E.P., Advances in ionospheric physics: roles, relevance and predictions in the system of solar-terrestrial plasmas, U.S. Natl. Rep. Int. Union Geod. Geophys. 1991-1994, Rev. Geophys., 721, 1995.

Szuszczewicz, E.P., et al., SUNDIAL: A world-wide study of interactive ionospheric processes and their roles in the transfer of energy and mass in the Sun-Earth system, Ann. Geophys., 6, 3, 1988.

Szuszczewicz, E.P., et al., Solar-terrestrial conditions during SUNDIAL '86 and empirical modeling of the global-scale ionospheric responses, Ann. Geophys., 8, 387, 1990.

Szuszczewicz, E.P., et al., Measurements and empirical model comparisons of F-region characteristics and auroral oval boundaries during the solstitial SUNDIAL campaign of 1987, Ann. Geophys., 11, 601-613, 1993.

Szuszczewicz, E.P., R.G. Roble, P.J. Wilkinson, and R. Hanbaba, Coupling mechanisms in the lower ionospheric-thermospheric system and manifestations in the formation and dynamics of intermediate and descending layers, J. Atmos. Terr. Phys., 57, 1483, 1995a.

Szuszczewicz, E.P., A. Mankofsky, P. Blanchard, C. Goodrich, D. McNabb, and D. Kamins, SAVS: A space and atmospheric visualization science system, in Visualization Techniques in Space and Atmospheric Sciences, edited by E.P. Szuszczewicz and J.H. Bredekamp, NASA SP-519, U.S. Gov Print Off., Washington, D.C., 1995b

Taylor, J.R., M. Lester, and T.K. Yeoman, A superposed epoch analysis of geomagnetic storms, Ann. Geophys., 12, 612 - 624, 1994.

Torr, M.R., D.G. Torr, P.G. Richards, and S.P. Yung, Mid- and low-latitude model of thermospheric emissions, 1, $O^+(^2P)$ 7320 A and N_2 (2P) 3371 A, J. Geophys. Res., 95, 21,147, 1990.

Torr, D.G., M.R. Torr, and P.G. Richards, Thermospheric airglow emissions: A comparison of measurements from ATLAS-1 and Theory, Geophys. Res. Lett., 20, 519, 1993.

Wilkinson, P.J., Scaling errors in ionospheric characteristics, Bull. 27, pp. 20-25, Ionosonde Network Advisory Group, U.S. Dep. Comm., Washington, D.C., 1978.

Wilkinson, P.J., E.P. Szuszczewicz, and R.G. Roble, Measurements and Modeling of Intermediate, Descending, and Sporadic Layers in the Lower Ionosphere: Results and Implications for Global-Scale Ionospheric-Thermospheric Studies, Geophys. Res. Lett., 19, 95, 1992.

Wilkinson, P., R.W. Schunk, R. Hanbaba, and H. Mori, Interhemispheric comparison of SUNDIAL *F* region data with global-scale ionospheric models, Ann. Geophys., 6, 31, 1988.

Wilkinson, P., P. Richards, K. Igarashi, Ionospheric climatology and weather in the Australian-Japanese sector during the SUNDIAL/ATLAS 1 campaign, J. Geophys. Res., this issue.

Yeoman, T.K., D.K. Milling, and D. Orr, Pi2 Polarization patterns on the U.K. Sub-auroral Magnetometer Network (SAMNET), Planet. Space Sci., 38, 589, 1990.

M. Abdu, Institutional Nacional de Pesquisas Espaciais, 201 Ari. Dos Astronautas, 1758, Sao Jose Dos Campos, Caipa Postal 515, Sao Paulo, Brazil, e-mail: abdu@dae.inpe.br

P. Blanchard and E.P. Szuszczewicz, Science Applications International Corporation, MS 2-3-1, 1710 Goodridge Drive, McLean, VA 22102, e-mail: blanchard@apo.saic.com; szusz@apo.saic.com

B. Emery, G. Lu, and R. Roble, National Center for Atmospheric Administration, 1850 Table Mesa Drive, Boulder, CO 80307, e-mail: emery@ncar.ucar.edu; roble@ncar.ucar.edu

D. Evans and J. Joselyn, National Oceanic and Atmospheric Administration, 325 Broadway, Boulder, CO 80303

R. Hanbaba, France Telecom/CNET, SPI F. 22301 Lannion, France, e-mail: rudi.hanbaba@lannion.cnet.fr

K. Igarashi, Communications Research Laboratory, Ministry of Posts and Telecommunications, 2-1 Nukui-Kitamachi 4-Chome, Tokyo, 184 Japan, e-mail: igarashi@crl.go.jp

P. Jiao, China Research Institute of Radio Propagation, P.O. Box 138/97, Xinxiang, Henan 453003, Ching, e-mail: crirp@mimi.cnc.ac.cn

M. Lester, Department of Physics, University of Leicester, Leicester, LE1 7RH England, e-mail: mle@uk.ac.le.ion

K. Miller, Center for Atmospheric and Space Science, University of Utah, Logan, UT 84322-4405

S. Pulinets, IZMIRAN, 142092 Troitsk, Moscow Region, Russia, e-mail: 193.232.24.52@charley.izmiran .rssi.ru

B.M. Reddy, National Physical Laboratory, Dr. K.S. Krishnan Road, New Delhi, India 110012

P. Richards and D. Torr, University of Alabama, Huntsville, AL 35899

P. Wilkinson, IPS Radio and Space Services, Level 4 15 Help Street, West Chatswood, * NSW, 2057 Australia, e-mail: phil@ips.gov.au

(Received September 6, 1995; revised April 26, 1996; accepted June 4, 1996.)